Imaging inter-valley coherent order in magic-angle twisted trilayer graphene

Hyunjin Kim, 1,2,3,* Youngjoon Choi,4,* Étienne Lantagne-Hurtubise,2,3 Cyprian Lewandowski,^{2,3,5,6} Alex Thomson,^{2,3,7,8} Lingyuan Kong,^{1,2} Haoxin Zhou,^{1,2} Eli Baum, ^{1,2} Yiran Zhang, ^{1,2,3} Ludwig Holleis, ⁴ Kenji Watanabe, ⁹ Takashi Taniguchi, Andrea F. Young, Jason Alicea, 3,7 and Stevan Nadi-Perge^{1,2,†} ¹T. J. Watson Laboratory of Applied Physics, California Institute of Technology, 1200 East California Boulevard, Pasadena, California 91125, USA ²Institute for Quantum Information and Matter, California Institute of Technology, Pasadena, California 91125, USA ³Department of Physics, California Institute of Technology, Pasadena, California 91125, USA ⁴Department of Physics, University of California at Santa Barbara, Santa Barbara, California 93106, USA ⁵National High Magnetic Field Laboratory, Tallahassee, Florida, 32310, USA ⁶Department of Physics, Florida State University, Tallahassee, Florida 32306, USA ⁷Walter Burke Institute for Theoretical Physics, California Institute of Technology, Pasadena, California 91125, USA ⁸Department of Physics, University of California, Davis, California 95616, USA ⁹National Institute for Materials Science, Namiki 1-1, Tsukuba, Ibaraki 305 0044, Japan

Magic-angle twisted trilayer graphene (MATTG) exhibits a range of strongly correlated electronic phases that spontaneously break its underlying symmetries^{1,2}. Here we investigate correlated phases of MATTG using scanning tunneling microscopy and identify striking signatures of interaction-driven spatial symmetry breaking. In low-strain samples, over a filling range of about 2-3 electrons or holes per moiré unit cell, we observe atomic-scale reconstruction of the graphene lattice that accompanies a correlated gap in the tunneling spectrum. This short-scale restructuring appears as a Kekulé supercell—implying spontaneous intervalley coherence between electrons—and persists in a wide range of magnetic fields and temperatures that coincide with the development of the gap. Large-scale maps covering several moiré unit cells further reveal a slow evolution of the Kekulé pattern, indicating that atomic-scale reconstruction coexists with translation symmetry breaking at the much longer moiré scale. We employ auto-correlation and Fourier analyses to extract the intrinsic periodicity of these phases and find that they are consistent with the theoretically proposed incommensurate Kekulé spiral order^{3,4}. Moreover, we find that the wavelength characterizing moiré-scale modulations monotonically decreases with hole doping away from half-filling of the bands and depends only weakly on the magnetic field. Our results provide essential insights into the nature of MATTG correlated phases in the presence of strain and imply that superconductivity emerges from an inter-valley coherent parent state.

Spontaneous symmetry breaking lies at the foundation of condensed matter physics, as the emergence of novel quantum phases often accompanies symmetry reduction. Superconductivity and magnetism provide canonical examples that emerge when charge conservation and spin-rotation symmetry are respectively broken. In the strongly correlated realm, superconductivity commonly occurs in conjunction with other forms of symmetry breaking^{5,6}, and unraveling their

^{*} These two authors contributed equally

[†] Correspondence: hyunjin@caltech.edu; s.nadj-perge@caltech.edu

intricate relation presents a profound challenge relevant for many platforms—including the growing family of twisted graphene multilayers^{1,2,7,8}. Scanning tunneling microscopy (STM) is a well-established tool for identifying certain symmetry-broken states, particularly those that leave direct signatures in real space via the local density of states distribution. Nevertheless, the inherently difficult task of creating large, sufficiently clean and low-strained areas in magic-angle twisted multilayers has so far hindered the ability of STM to generate spatial maps of electronic structures sufficient for unambiguously diagnosing microscopic symmetry-breaking order. Previous studies have, therefore, focused mostly on observing spectroscopic signatures combined with basic structural characterization^{9–12}, especially in the context of MATTG^{13,14}. Only very recently, this challenge has been resolved in twisted bilayers¹⁵, while MATTG has not been explored in the context of symmetry-breaking orders.

Fig. 1a sketches the STM measurement setup and the structure of twisted trilayer graphene where the second layer is twisted by the angle θ , and the first and third layers are aligned. This configuration is known to exhibit an electronic structure that, in the absence of a perpendicular electric field, hosts twisted bilayer graphene-like flat bands and an additional set of dispersive Dirac cones ^{16,17}. We focus on an area with low heterostrain ($\epsilon \approx 0.12\%$) and twist angle $\theta = 1.60^{\circ}$, close to the magic-angle value for TTG (see Methods and Extended Data Fig. 1 and Extended Data Fig. 2 for fabrication details). High-resolution imaging resolving the atomic scale of TTG near an AAA site—for which carbon atoms on all three layers are aligned (Fig. 1b,c)—reveals a honeycomb structure with 0.246 nm lattice constant accompanied by a more subtle larger-scale atomic modulation. This modulation, while visible in topography, is more prominent in the dI/dV spatial maps (Fig. 1d,e) that show a clear lattice tripling pattern, the intensity of which depends sensitively on the applied bias voltage $V_{\rm Bias}$, with the contrast approximately inverting upon changing the sign of V_{Bias} (see Extended Data Fig. 3). Fourier analysis of the dI/dV maps further confirms the periodicity of this pattern (Fig. 1f): a set of six outer peaks corresponding to the graphene lattice is accompanied by six inner peaks that correspond to $1/\sqrt{3}$ of the graphene reciprocal lattice vectors rotated by 30°. This enlargement of the graphene unit cell into a 30°-rotated $\sqrt{3} \times \sqrt{3}$ supercell corresponds to a so-called Kekulé distortion previously observed in monolayer graphene decorated with metallic adatoms¹⁸ or in the quantum Hall regime^{19,20}. In general, the observation of Kekulé distortion implies a reduction of the Brillouin zone arising from a coherent scattering of electrons between the K and K' valleys, commonly referred to as inter-valley coherence.

The observed Kekulé distortion strongly depends on gate voltage, i.e., filling (Fig. 2). Focusing still on the vicinity of the AAA sites, when the MATTG Fermi level is in the remote bands (Fig. 2a,e) or near charge neutrality (Fig. 2c,g), the Kekulé distortion is completely absent. In contrast, a very prominent distortion arises at filling factors of around $-3 < \nu < -2$ (Fig. 2b,f) and $2 < \nu < 3$ (Fig. 2d,h). Fig. 2i summarizes the observed relative Kekulé peak intensity compared to the graphene lattice peaks. Strikingly, the regions of non-zero intensity match well with the regions that host either an insulating gap or pseudogap in the gate spectroscopy (Fig. 2j; see also Extended Data Fig. 9 for data on another sample). The relative intensity of the Kekulé peaks depends strongly on the bias voltage and is approximately maximized when $V_{\rm Bias}$ matches the LDOS peak accompanying the (pseudo) gap (see Extended Data Fig. 3). Moreover, at higher temperatures, as the gap is suppressed, the visibility of Kekulé peaks also diminishes (Extended Data Fig. 4). Strong dependence of the reconstruction on $V_{\rm Gate}$, $V_{\rm Bias}$ and the temperature indicate its electronic origin and rule out the possibility that the observed Kekulé peaks arise from impurities or structural deformations.

Various inter-valley coherent (IVC) phases have been theoretically proposed as the ground state of magic-angle twisted bilayers^{3,21–23}, with a limited number of theoretical calculations specific to

MATTG²⁴. We consider the family of such candidate IVC phases, motivated by Ref. 25,26 and the close band-structure and spectroscopic resemblances between twisted bilayers and trilayers. One member of this family—dubbed the Kramers IVC phase—was predicted to appear in unstrained samples^{21–23} and manifests as a magnetization density wave that generates Kekulé peaks in the LDOS only at finite magnetic fields^{25,26}. Since we observe pronounced Kekulé peaks already at zero magnetic field, this IVC order can be ruled out in our MATTG samples. Two other leading candidates include the time-reversal-symmetric IVC (T-IVC) and incommensurate Kekulé spiral (IKS) phases; both produce charge density waves that generate LDOS Kekulé peaks at zero magnetic field, compatible with our measurements.

To establish more precisely the nature of the correlated state, we investigate variations of the Kekulé pattern across neighboring moiré unit cells by taking large-area dI/dV maps (taken at $\nu=-2.3$) covering a 36 nm \times 36 nm region that encompasses twenty moiré AAA sites (Fig. 3a). Focusing first on two regions around neighboring AAA sites (Fig. 3b,e, marked by a yellow and blue square in Fig. 3a), we decompose the map using Fourier transform (FT) based filtering to separate the spatial evolution of the Kekulé distortions from the underlying graphene lattice; see methods for details. These regions are chosen to have graphene lattices precisely atomically aligned (Fig. 3c,f). Under these conditions, while the raw data show only subtle differences, FT-filtered Kekulé patterns clearly show that bright spots (high intensity) in the yellow window (Fig. 3d) become dark spots (low intensity) in the blue window (Fig. 3g) and vice-versa. This dichotomy establishes that the Kekulé distortion between two neighboring moiré sites changes significantly. We note that, in general, the intensity of the Kekulé distortion FT peaks and graphene reciprocal lattice peaks evolve independently across the sample.

To quantify the spatial variation across the entire mapped region, we extend the above method and create Kekulé auto-correlation maps (Fig. 3h). Here, we fix a small region of approximately 1 nm × 1 nm and separately auto-correlate graphene lattice- and Kekulé-filtered periodicities with a 'moving window' of the same size that samples different map regions. The auto-correlation is normalized such that perfectly correlated regions correspond to 1 while perfectly anti-correlated regions correspond to -1. We assign Kekulé auto-correlation values to the nearest points at which atomic auto-correlation exceeds a threshold of one-half (the conclusions do not depend on the exact threshold value). This procedure ensures alignment of the underlying graphene lattices when comparing Kekulé modulation across different parts of the map. The zoom-in to the Fig. 3h map reveals a rapid evolution of the auto-correlation and the atomic scale lattice tripling (3-unit cell) pattern (Fig. 3i,j,k,l; see methods for further discussion). On the moiré length scale, this Kekulé map shows clear stripe-like red-blue patterns along the l_1 and l_2 directions but shows weak dependence along the l_3 direction. The observed periodicity reflects modulation at a wavevector $q_{\text{Kekul\acute{e}}}$ that is perpendicular to the l_3 direction with a magnitude that is approximately half of a moiré reciprocal lattice vector (for this filling factor)—corresponding to a near doubling of the moiré unit cell.

While the auto-correlation analysis shown above demonstrates that translation symmetry on the moiré length scales is broken, obtaining the modulation periodicity directly from real space maps is challenging when the order is far from commensurate. We, therefore, turn to a Fourier-space analysis to extract the modulation wavevectors arising over a broad filling range. Fig. 4a shows the Fourier transform of the map shown in Fig. 3a. In contrast to the FT images of the small real-space areas, here the graphene reciprocal lattice and Kekulé peaks are decorated by satellite peaks—reflecting the longer wavelength moiré pattern in the original image. Identifying the exact graphene lattice vector peak among the cluster of satellite peaks is non-trivial, as even small errors in the STM calibration or possible homostrain effects within the top graphene layer

can alter it. We overcome this problem by examining the higher-order reciprocal lattice vectors, which exhibit smaller clusters in Fourier space and thus allow for more precise extraction (see Extended Data Fig. 6). In Fig. 4b-d, we mark the exact position of the graphene reciprocal lattice vectors $G_{1,2,3}$. Next, based on these vectors, we can accurately estimate the positions of the FT peaks that would arise for a uniform Kekule pattern on the graphene scale as $K_1 = (G_1 + G_2)/3$, $K_2 = (G_2 + G_3)/3$, and $K_3 = (G_3 - G_1)/3$ (blue circles in Fig. 4e-g). None of the satellite peaks in the FT signal line up with $K_{1,2,3}$, though crucially, the observed displacement of all three sets of peaks relative to $K_{1,2,3}$ can be accounted for by a *single* wavevector $q_{\text{Kekulé}}$.

The extracted Kekulé modulation wavevector $q_{\rm Kekul\acute{e}}$ does not change with $V_{\rm Bias}$ but evolves monotonically with $V_{\rm Gate}$, and is generally incommensurate with the moiré potential. Remarkably, upon hole doping from $\nu=-2$ to -2.5, $q_{\rm Kekul\acute{e}}$ always points along the g_3 moiré reciprocal lattice vector within error bars (Fig. 4i) but increases in magnitude, eventually crossing the moiré Brillouin zone boundary near the commensurate point $g_3/2$ (Fig. 4l). Note that these results are consistent with the real-space auto-correlation analysis in Fig. 3. Furthermore, the observed modulation is quite robust to magnetic fields: By performing similar mappings in moderate (2T) and high (8T) out-of-plane magnetic fields we find that spatially varying Kekulé distortions are still present (Extended Data Fig. 5) and that $q_{\rm Kekul\acute{e}}$ only slightly shifts its direction from its zero field value. Finally, our procedure gives consistent results for $q_{\rm Kekul\acute{e}}$ for maps with different sizes and taken at various $V_{\rm Bias}$.

We now discuss the implications of our observations for the nature of the correlated state between $\nu=-2$ and -2.5. The identification of a Kekulé pattern modulating slowly with a generally incommensurate, doping-dependent wavevector suggests the presence of IKS order. Theoretically, the IKS state arises out of an inter-valley nesting instability at a single wavevector $q_{\rm IKS}$ in the presence of small heterostrain ($\sim 0.1-0.2\%$)^{3,4,27}—comparable to the values of our MATTG samples. The resulting order yields a lattice-tripling pattern that slowly varies between moiré lattice sites with wavelength $2\pi/|q_{\rm IKS}|$ along a direction set by $q_{\rm IKS}$ (see Fig. 4h and Supplementary Information (SI) for more discussion and theoretical modeling). Importantly, this vector is distinct from the extracted modulation wavevector $q_{\rm Kekulé}$: whereas $q_{\rm IKS}$ characterizes variations relative to the moiré lattice, $q_{\rm Kekulé}$ instead measures the modulation of the lattice-tripling order relative to the graphene lattice. The two vectors are related by a momentum shift that connects the mini-BZ center γ and the mini-BZ corners κ (see schematic in Fig. 4 h).

Because IKS order arises from an inter-valley nesting instability, it is greatly influenced by the structure of the flat bands³ —especially the location of the flat-band maxima and minima at each valley. In the continuum model^{28,29}, the valence flat-band minima and maxima respectively occur at the moiré Brillouin zone γ and κ , κ' points. Upon inclusion of heterostrain, such features are distorted in a non-universal fashion that depends on the strain angle and magnitude. Electronic interactions, which significantly alter the shape of the flat bands, are also crucial to determine the preferred IKS instability. Charge inhomogeneity, characterized by the self-consistent Hartree term, tends to invert flat bands around the γ point^{30–35}. Good agreement with the experiment is found when interaction-induced band inversion is not pronounced. In this case, theoretically extracted $q_{\rm Kekul\acute{e}}$ that includes measured heterostrain matches well with the observations, within the error bars of both the experimental extraction and the theoretical procedure (see SI for details). The calculated modulation wavevector $oldsymbol{q}_{ ext{Kekul\'e}}$ evolves with hole doping away from u=-2 following experimentally observed trends, with the evolution being more pronounced in the non-inverted regime. Incorporating a perpendicular displacement field induced by the back gate, which hybridizes the twisted bilayer graphene-like flat bands of MATTG with the Dirac cone (see SI Sec. 2), leaves the theoretically extracted $q_{\text{Kekulé}}$ largely unchanged (SI Fig. 6). Finally, we note that the measured pattern in Fig. 3 appears very close to a *commensurate* modulation; see SI Sec. 9 for a possible mechanism favoring a lock-in of the IKS modulation to a nearby commensurate wavevector.

Our experiments reveal several other signatures directly related to symmetry breaking in MATTG. In many of the FT maps, we observed suppression of the FT satellite peaks along narrow striped regions, forming a 'sash-like' feature (see white arrows in Fig. 4a) discussed theoretically in Ref. 25 in the context of C_3 symmetry breaking (see also Extended Data Fig. 7). These sashes are resolved at various filling factors both within the graphene reciprocal lattice vector peaks and Kekulé peaks; moreover, consistent with C_3 symmetry breaking on the graphene lattice scale, they do not appear in all directions of the FT maps. This observation is compatible with the IKS ground state around $\nu = -2$. Interestingly, similar features are observed near charge neutrality for $V_{\rm Gate} = 0$ V, where we did not detect lattice tripling order. For this gate voltage, we further observed a preferred directionality in graphene bonds and a spatial evolution of the dI/dV signal near the AAA site that is consistent with a nematic semi-metallic ground state²⁵ (Extended Data Fig. 10). These findings further highlight the ability of STM to distinguish various symmetry-broken ground states in moiré heterostructures.

Finally, our spectroscopic detection and characterization of IVC order provide fresh insight into the puzzle surrounding the origin of superconductivity and the accompanying pseudogap phase in MATTG. The emergence of inter-valley coherence at fillings where we previously reported unconventional superconductivity¹³ (see Extended Data Fig. 9) sharply constrains theoretical scenarios. Further constraints follow from the surprising observation that the strength of IVC order, quantified by the normalized Kekulé peak intensity, is maximal in the pseudogap regime (around $\nu \approx -2.3$ to -2.5) instead of the $\nu = -2$ insulating phase. Other enigmatic properties of MATTG have also been observed in this filling range, including the evolution from U- to V-shaped tunneling spectra observed spectroscopically¹³, as well as a sharp change in the Ginzburg-Landau coherence length and maximal critical temperature observed in transport^{1,2}. Linking these diverse aspects of MATTG phenomenology poses an outstanding challenge for future theory and experiments. Another interesting open question is how prevalent the IVC order among the strongly correlated graphene-based systems is as it is found not only in magic-angle bilayers¹⁵ and now trilayers but also in graphene itself at high magnetic fields^{19,20}.

[1] Park, J. M., Cao, Y., Watanabe, K., Taniguchi, T. & Jarillo-Herrero, P. Tunable strongly coupled superconductivity in magic-angle twisted trilayer graphene. *Nature* **590**, 249–255 (2021).

^[2] Hao, Z. *et al.* Electric field–tunable superconductivity in alternating-twist magic-angle trilayer graphene. *Science* **371**, 1133–1138 (2021).

^[3] Kwan, Y. *et al.* Kekulé spiral order at all nonzero integer fillings in twisted bilayer graphene. *Physical Review X* **11**, 041063 (2021).

^[4] Wagner, G., Kwan, Y. H., Bultinck, N., Simon, S. H. & Parameswaran, S. A. Global Phase Diagram of the Normal State of Twisted Bilayer Graphene. *Physical Review Letters* **128**, 156401 (2022).

^[5] Fradkin, E., Kivelson, S. A. & Tranquada, J. M. Colloquium: Theory of intertwined orders in high temperature superconductors. *Reviews of Modern Physics* **87**, 457–482 (2015).

^[6] Fernandes, R. M. *et al.* Iron pnictides and chalcogenides: A new paradigm for superconductivity. *Nature* **601**, 35–44 (2022).

^[7] Zhang, Y. *et al.* Promotion of superconductivity in magic-angle graphene multilayers. *Science* **377**, 1538–1543 (2022).

- [8] Park, J. M. *et al.* Robust superconductivity in magic-angle multilayer graphene family. *Nature Materials* **21**, 877–883 (2022).
- [9] Kerelsky, A. *et al.* Maximized electron interactions at the magic angle in twisted bilayer graphene. *Nature* **572**, 95–100 (2019).
- [10] Choi, Y. *et al.* Electronic correlations in twisted bilayer graphene near the magic angle. *Nature Physics* **15**, 1174–1180 (2019).
- [11] Xie, Y. *et al.* Spectroscopic signatures of many-body correlations in magic-angle twisted bilayer graphene. *Nature* **572**, 101–105 (2019).
- [12] Jiang, Y. *et al.* Charge order and broken rotational symmetry in magic-angle twisted bilayer graphene. *Nature* **573**, 91–95 (2019).
- [13] Kim, H. *et al.* Evidence for unconventional superconductivity in twisted trilayer graphene. *Nature* **606**, 494–500 (2022).
- [14] Turkel, S. *et al.* Orderly disorder in magic-angle twisted trilayer graphene. *Science* **376**, 193–199 (2022).
- [15] Nuckolls, K. P. *et al.* Quantum textures of the many-body wavefunctions in magic-angle graphene. *Nature* **620**, 525–532 (2023).
- [16] Khalaf, E., Kruchkov, A. J., Tarnopolsky, G. & Vishwanath, A. Magic angle hierarchy in twisted graphene multilayers. *Physical Review B* **100**, 085109 (2019).
- [17] Carr, S. *et al.* Ultraheavy and Ultrarelativistic Dirac Quasiparticles in Sandwiched Graphenes. *Nano Letters* **20**, 3030–3038 (2020).
- [18] Gutiérrez, C. *et al.* Imaging chiral symmetry breaking from Kekulé bond order in graphene. *Nature Physics* **12**, 950–958 (2016).
- [19] Liu, X. *et al.* Visualizing broken symmetry and topological defects in a quantum Hall ferromagnet. *Science* **375**, 321–326 (2022).
- [20] Coissard, A. *et al.* Imaging tunable quantum Hall broken-symmetry orders in graphene. *Nature* **605**, 51–56 (2022).
- [21] Kang, J. & Vafek, O. Strong Coupling Phases of Partially Filled Twisted Bilayer Graphene Narrow Bands. *Physical Review Letters* **122**, 246401 (2019).
- [22] Bultinck, N. *et al.* Ground State and Hidden Symmetry of Magic-Angle Graphene at Even Integer Filling. *Physical Review X* **10**, 031034 (2020). 1911.02045.
- [23] Lian, B. *et al.* Twisted bilayer graphene. IV. Exact insulator ground states and phase diagram. *Physical Review B* **103**, 205414 (2021).
- [24] Christos, M., Sachdev, S. & Scheurer, M. S. Correlated Insulators, Semimetals, and Superconductivity in Twisted Trilayer Graphene. *Physical Review X* **12**, 021018 (2022).
- [25] Hong, J. P., Soejima, T. & Zaletel, M. P. Detecting Symmetry Breaking in Magic Angle Graphene Using Scanning Tunneling Microscopy. *Physical Review Letters* **129**, 147001 (2022).
- [26] Călugăru, D. *et al.* Spectroscopy of Twisted Bilayer Graphene Correlated Insulators. *Physical Review Letters* **129**, 117602 (2022).
- [27] Wang, T. *et al.* Kekulé spiral order in magic-angle graphene: a density matrix renormalization group study (2022). 2211.02693.
- [28] Lopes dos Santos, J. M. B., Peres, N. M. R. & Castro Neto, A. H. Graphene Bilayer with a Twist: Electronic Structure. *Physical Review Letters* **99**, 256802 (2007).
- [29] Bistritzer, R. & MacDonald, A. H. Moiré bands in twisted double-layer graphene. *Proceedings of the National Academy of Sciences* **108**, 12233–12237 (2011).
- [30] Guinea, F. & Walet, N. R. Electrostatic effects, band distortions, and superconductivity in twisted graphene bilayers. *Proceedings of the National Academy of Sciences* **115**, 13174–13179 (2018).

- [31] Cea, T., Walet, N. R. & Guinea, F. Electronic band structure and pinning of Fermi energy to Van Hove singularities in twisted bilayer graphene: A self-consistent approach. *Physical Review B* **100**, 205113 (2019).
- [32] Cea, T. & Guinea, F. Band structure and insulating states driven by Coulomb interaction in twisted bilayer graphene. *Physical Review B* **102**, 045107 (2020).
- [33] Rademaker, L., Abanin, D. A. & Mellado, P. Charge smoothening and band flattening due to Hartree corrections in twisted bilayer graphene. *Physical Review B* **100**, 205114 (2019).
- [34] Goodwin, Z. A. H., Vitale, V., Liang, X., Mostofi, A. A. & Lischner, J. Hartree theory calculations of quasiparticle properties in twisted bilayer graphene. *Electronic Structure* **2**, 034001 (2020). 2004.14784.
- [35] Xie, M. & MacDonald, A. H. Weak-Field Hall Resistivity and Spin-Valley Flavor Symmetry Breaking in Magic-Angle Twisted Bilayer Graphene. *Physical Review Letters* **127**, 196401 (2021).
- [36] Choi, Y. *et al.* Correlation-driven topological phases in magic-angle twisted bilayer graphene. *Nature* **589**, 536–541 (2021).
- [37] Choi, Y. *et al.* Interaction-driven band flattening and correlated phases in twisted bilayer graphene. *Nature Physics* **17**, 1375–1381 (2021).

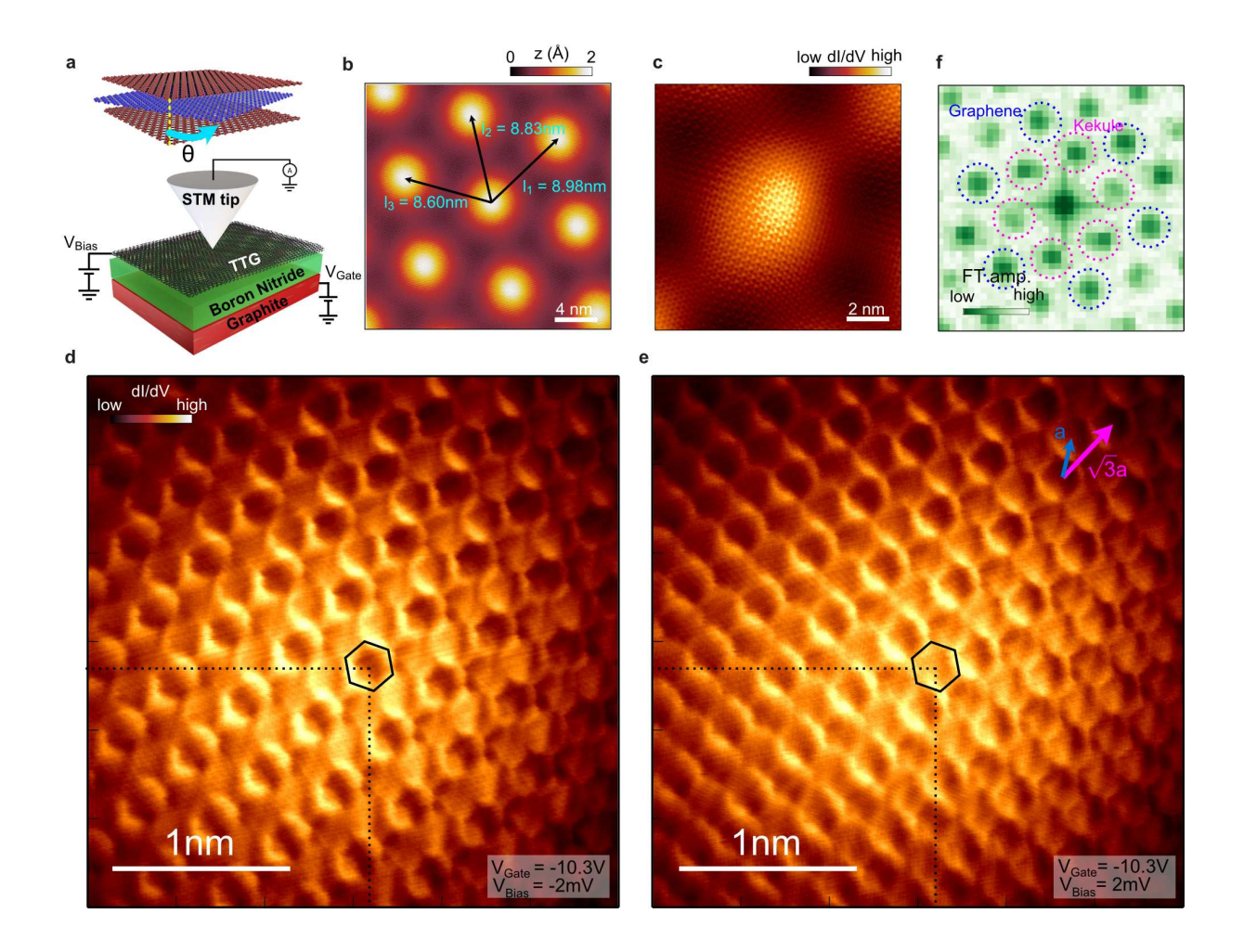


Fig. 1. Overview of the experiment and atomically resolved maps revealing Kekulé pattern. a, Schematic depicting twisted trilayer graphene (up) and device geometry used for the STM measurements (down). b, Atomically resolved topography showing the moiré lattice used to extract hetero-strain magnitude $|\epsilon| \approx 0.12\%$ and twist angle $\theta = 1.60^\circ$. c, Tunneling conductance map taken at $V_{\rm Gate} = -9{\rm V}$ and $V_{\rm Bias} = -2{\rm mV}$ at the AAA site showing atomic resolution. d, e, dI/dV map measured at fixed $V_{\rm Gate} = -10.3V$ at negative $V_{\rm Bias} = -2{\rm mV}$ (d) and positive $V_{\rm Bias} = 2{\rm mV}$ (e) further zoom in into AAA site and showing contrast inversion upon change of $V_{\rm Bias}$. f, Fourier transformation of Fig. 1d showing well-resolved peaks corresponding to graphene lattice and Kekulé reconstruction. Data in panels d and e were taken at T = 400 mK. Unless otherwise specified, data is taken at T = 2 K.

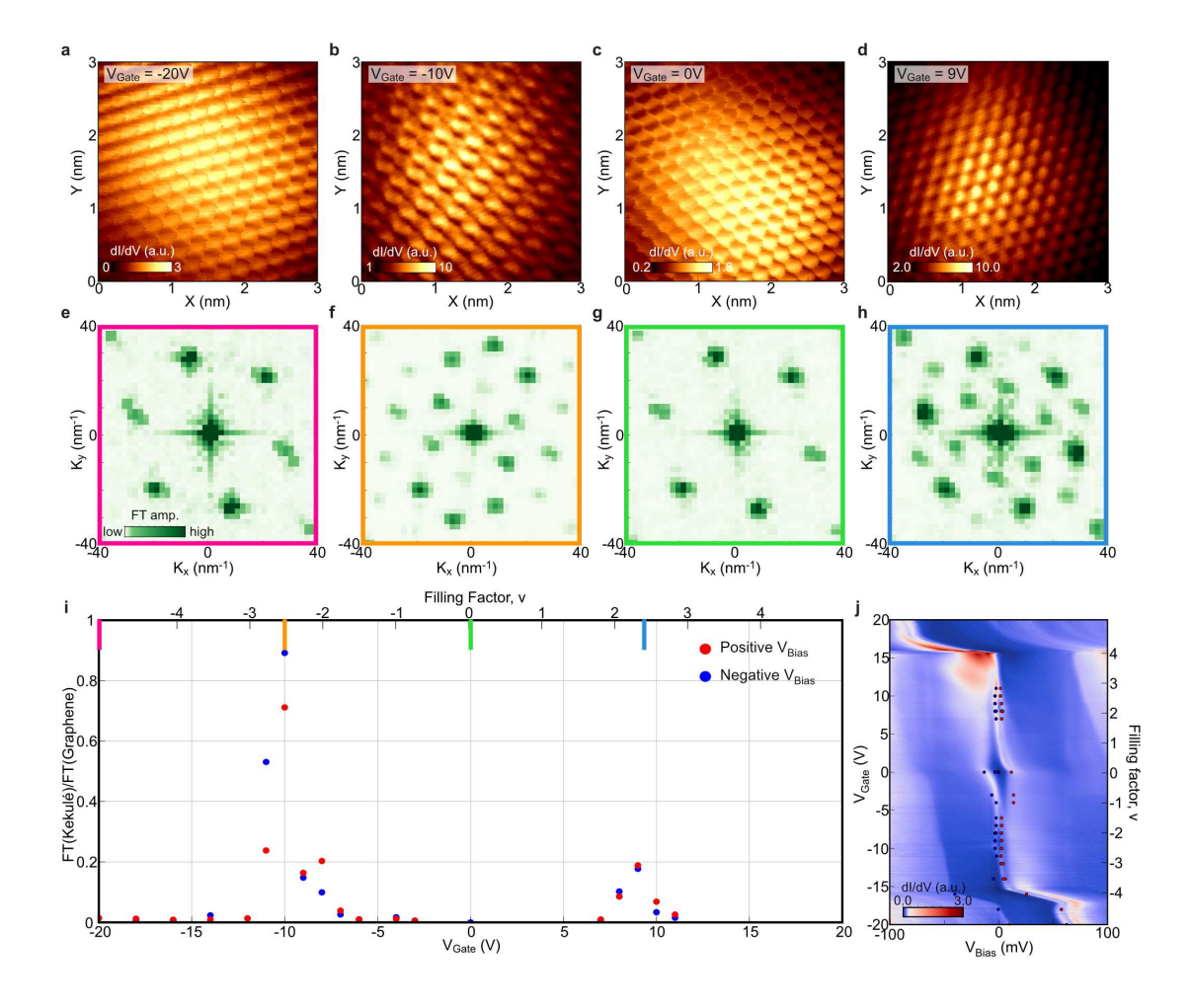


Fig. 2. $V_{\rm Gate}$ dependent mapping of Kekulé order on MATTG. a-d, Real space dI/dV map at $V_{\rm Gate} = -20 {\rm V}$ (a), $-10 {\rm V}$ (b), $0 {\rm V}$ (c), $9 {\rm V}$ (d), taken at $V_{\rm Bias} = 63 {\rm mV}$ (a), $-3 {\rm mV}$ (b), $-13 {\rm mV}$ (c), $3 {\rm mV}$ (d), tracking the evolution of the flat band density of states. e-h, Fourier transformation of Fig. 2a-d zoomed in to show the peaks corresponding to graphene and Kekulé reciprocal lattice vectors. In addition to graphene and Kekulé peaks, in panels f and h we also clearly resolve higher-order peaks. i, Intensity of the peaks at Kekulé reciprocal lattice vector normalized by the intensity of the peaks at graphene reciprocal lattice vector as a function of $V_{\rm Gate}$. The intensities at all six Kekulé peaks are summed up and divided by the sum of six graphene peak intensities. Blue and red dots correspond to averaged data across positive (negative) $V_{\rm Bias}$ values for each $V_{\rm Gate}$ (all the values are marked in Fig. 2j). j, $V_{\rm Gate}$ dependent dI/dV spectroscopy measured on the same area where Fig. 2a-h is measured.

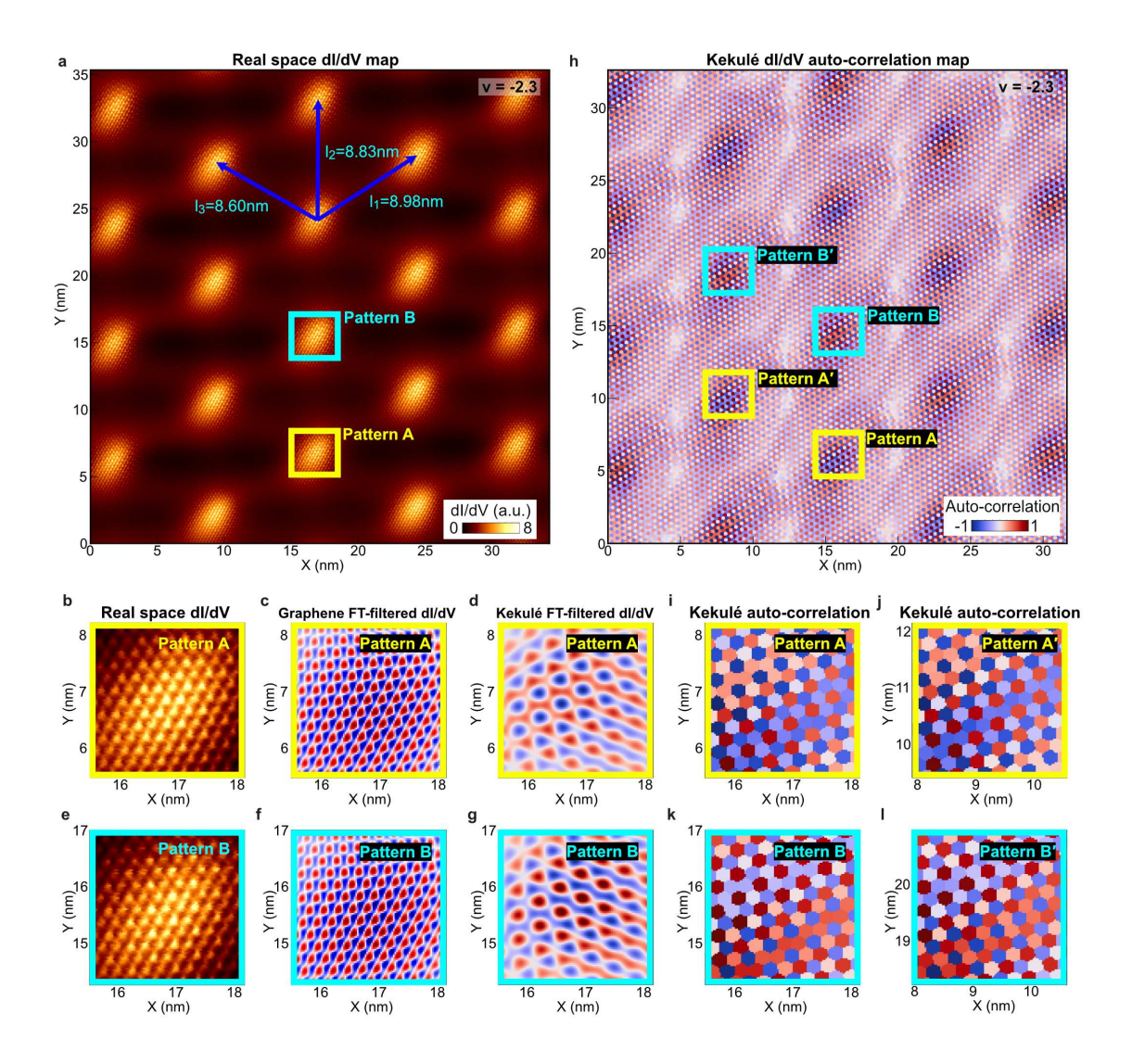


Fig. 3. Evidence of moiré translation symmetry breaking. a, Large-scale area dI/dV scan around $\nu=-2.3$. b,e, 2.2 nm \times 2.2 nm window from Fig. 3a centered around one AAA site (b) and its nearest neighbor AAA site along l_2 direction (e). c,f, Corresponding graphene FT filtered dI/dV map for Fig. 3b,e shows the precise alignment of the atomically resolved signals. d,g, Kekulé FT filtered dI/dV map for Fig. 3b,e exhibiting inverted contrast between neighboring AAA sites. FT filtering for graphene (Kekulé) signals are performed by masking the FT image with round masks of 3.5nm⁻¹ radius around six graphene (Kekulé) FT peaks and do inverse FT. h, Kekulé dI/dV auto-correlation map of Fig. 3a. Auto-correlation is calculated between two small windows from Fig. 3a where one window is fixed at some position and the other spans the image. (see also the Methods section) i,j, 2.2 nm by 2.2 nm window taken from Kekulé auto-correlation map centered around AAA site showing pattern A (i) and neighboring AAA site along l_3 direction showing almost similar pattern (j). k,l, 2.2 nm by 2.2 nm window taken from Kekulé auto-correlation map centered around AAA site showing pattern B (k) and neighboring AAA site along l_3 direction showing almost similar pattern (l).

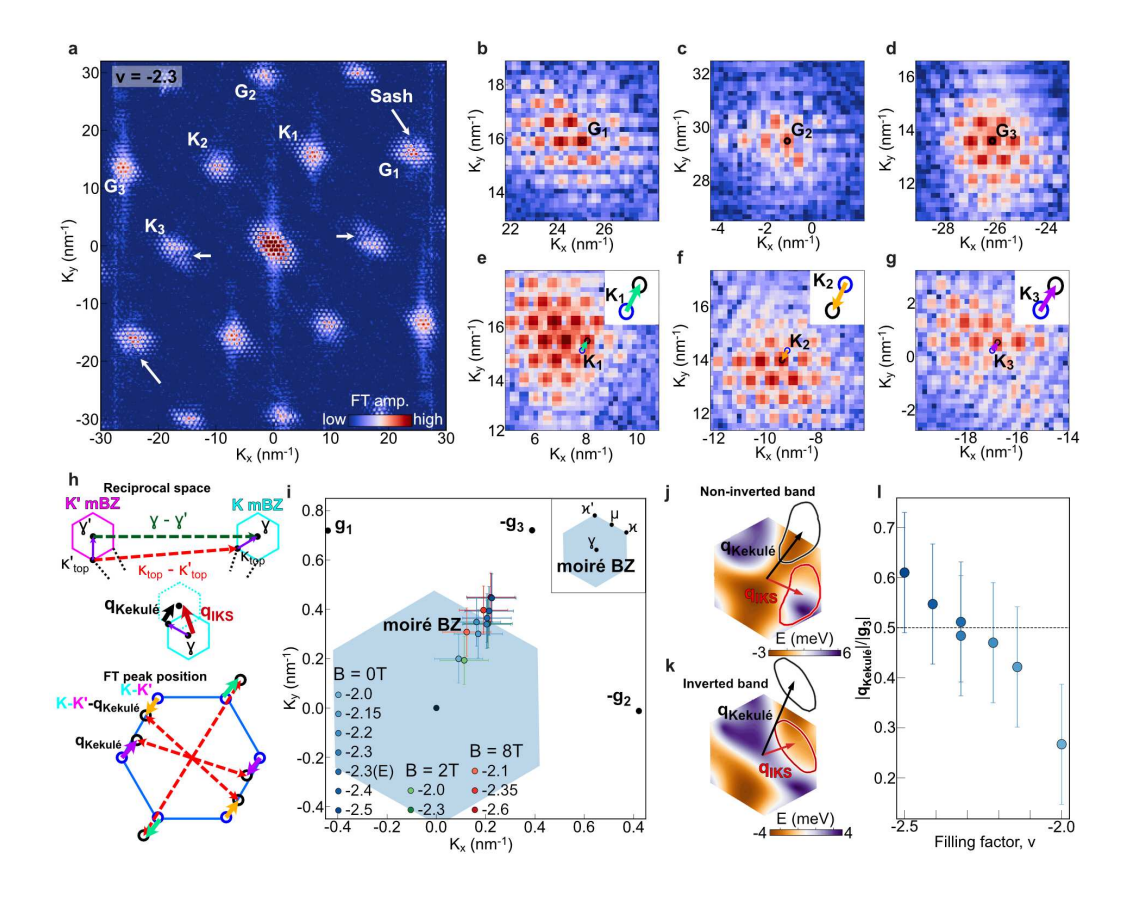


Fig. 4. Incommensurate Kekulé spiral wavevector extracted from the Fourier transformation maps.

a, Fourier transformation of the real space dI/dV map at $\nu=-2.3$ and $V_{\rm Bias}=-2$ mV. Fourier transform peaks at graphene reciprocal lattice vector site is decorated with moiré satellite peaks are named G_1, G_2, G_3 , while peaks around Kekulé reciprocal lattice vector position are named K_1, K_2, K_3 . **b-d**, Zoom-in images of Fig. 4a where exact graphene reciprocal lattice vector positions are marked as black dots. e-g, Zoom-in images of Fig. 4a around K_1 , K_2 , K_3 , where expected Kekulé reciprocal lattice vector positions are marked as black circles. The nearest satelite peaks that are used to extract the modulation wavevector $q_{
m Kekul\acute{e}}$ are marked as blue circles. Arrows denote the direction of $q_{\text{Kekul\'e}}$ for each K_1, K_2, K_3 . h, Schematics depicting the hybridization of K and K' moiré BZ for two different cases (upper panel). γ to γ' (green vector) gives Kekulé pattern that is commensurate with the moiré lattice while κ_{top} to κ'_{top} (red vector) gives spatially uniform Kekulé pattern on the graphene scale. Middle panel shows the relation between $q_{\rm IKS}$ and $q_{\rm Kekulé}$. Lower panel shows schematics of FT peaks corresponding to inter-valley coherent state with finite Kekulé modulation $q_{\rm Kekul\acute{e}}$. i, Extracted modulation wavevector $q_{\rm Kekul\acute{e}}$ as a function of both $V_{\rm Gate}$ and out-ofplane magnetic field of 2T and 8T. Black dots denote the positions of moiré reciprocal lattice vectors g_1, g_2 , g_3 , which are perpendicular to l_1 , l_2 , l_3 (respectively) in Fig. 1b. Blue hexagon is the moiré Brillouin zone (mBZ) calculated with the g_1 , g_2 , g_3 extracted from the experiment. j and k, Calculated band structure of the top-most valence-band in valley K at filling $\nu = -2$, in the regime of small Hartree correction ($\epsilon_r = 30$, panel j), where the flat band is non-inverted, and in the regime of large Hartree correction ($\epsilon_r = 15$, panel **k**), where the flat band is inverted around the γ point of the mBZ. The black and red arrows respectively indicate the theoretically optimal $q_{\text{Kekul\acute{e}}}$ and q_{IKS} wavevectors, with contours showing the corresponding confidence interval (see SI Section 5 for details.) I, Size of $q_{\text{Kekul\'e}}$ normalized by the size of the moiré reciprocal lattice vector g_3 which is almost aligned with $q_{\text{Kekul\'e}}$. Error bars are set by the pixel size in **b-g** (see Methods). The black dashed line displays the mBZ boundary.

Methods:

Device fabrication: To fabricate the graphite/hBN/TTG device, the layers are first picked up sequentially using a poly(bisphenol A carbonate) (PC) film on a polydimethylsiloxane (PDMS) block via the typical dry transfer technique at temperatures between 60-100°C. The stack then needs to be 'flipped' onto a substrate to expose the TTG and electrically contacted it without introducing polymer residues.

Stack flipping is accomplished using a gold-coated PDMS slide, as shown in Extended Data Fig. 1a-f. In this step, the PC film initially supporting the stack is peeled off of the PDMS slide and transferred stack-side down onto PDMS block coated with Ti/Au (3/12nm) via e-beam evaporation. The PC film is then removed using N-methyl-2-pyrrolidone (NMP). The gold surface and the stack are naturally sealed together, preventing the NMP from permeating the interface containing the TTG. Moreover, the evaporated metals prevent any residues from contacting the sample surface. Because the stiction between gold and the van der Waals stack is weaker that between the van der Waals stack and silica, the stack can then be 'dropped' onto an oxide substrate without the need for further solvent use.

To apply bias and gate voltages to the sample without contaminating the surface, we use a 'gold stamping' technique illustrated in Extended Data Fig. 1g-k. First, a SU8 (SU-8 2005, Microchem) photoresist mold is defined on a silicon oxide substrate. Then, PDMS (SYLGARD 184, 10:1) is poured onto the mold and dried, resulting in a patterned stamp after peeling it off from the mold. Gold is evaporated (e-beam evaporation, 10 - 20nm) onto the PDMS stamp, which is then pressed down onto the desired area of the sample at $130^{\circ}C$. As only the highest parts of the stamp make contact with the sample—leaving gold behind— the rest of the sample surface remains uncontaminated.

Samples B and C were prepared using our previously developed 'PDMS assisted flipping' technique¹⁰. The hBN/MATTG stack is picked up using a PC film, peeled off, and flipped onto an intermediate PDMS block. The PC film is then washed away with NMP/isopropyl alcohol and kept under a vacuum for several days. The stack is subsequently transferred onto a graphite gate that has been previously dropped on a substrate. Lastly, a graphite contact is exfoliated on PDMS and dropped to connect MATTG to a pre-patterned electrode.

To compare the quality of sample A to B, we used AFM in AC tapping mode (Extended Data Fig. 2). Sample B exhibited residues on the surface, which became apparent after scanning (cleaning) an area with contact mode due to the appearance of square residue boundaries. However, no signs of residues were observed on sample A before or after scanning the area with contact mode. Once a sample was fabricated, no further annealing was conducted inside the STM chambers.

Conductive AFM Characterization at Room Temperature: Conductive Atomic Force Microscopy (cAFM) is a powerful imaging technique used for visualizing moiré patterns in twisted heterostructures, as reported in various studies?? We employed cAFM to characterize the twist angles and cleanliness of a sample at room temperature prior to cooling it down for STM measurements. A commercial AFM (Asylum Research Cypher) equipped with a conducting tip (ASYELEC-01-R2 from Asylum Research, with a spring constant of approximately 2.8N/m) is utilized. During cAFM imaging, bias voltage of 100mV was typically applied between the tip and the twisted graphene, while the gate was left floating. The typical magic angle twisted trilayer graphene sample exhibits moiré pattern surrounded by supermoiré stripes, as previously reported in the literature (Extended Data Fig. 2c,f). The region with a moiré wavelength of approximately 9 nm, which corresponds to the magic angle of twisted trilayer graphene, was the target during the navigation of the STM tip to the sample.

STM measurements: The STM measurements were performed in a Unisoku USM 1300J

STM/AFM system using a Platinum/Iridium (Pt/Ir) tip as in our previous works on bilayers 10,36,37 . All reported features are observed with many (usually at least ten) different microtips. Unless specified otherwise, data was taken at temperature T=2 K and the parameters for dI/dV spectroscopy measurements were $V_{\rm Bias}=100$ mV and I=1 nA, and the lock-in parameters were modulation voltage $V_{\rm mod}=0.2-1$ mV and frequency f=973 Hz. Real space dI/dV maps are taken with the constant height mode (feedback turned off, tilt corrected). The piezo scanner is calibrated on a Pb(110) crystal and verified by measuring the distance between carbon atoms. The twist-angle uncertainty is approximately $\pm 0.01^{\circ}$, and is determined by measuring moiré wavelengths from topography. Filling factor assignment has been performed by taking Landau fan diagrams as discussed previously 36 or by identifying features corresponding to full-filling and CNP LDOS suppression 10 in data sets where magnetic field dependence was not studied. The deviations between the two methods in assigning filling factors are typically within 5%.

The gate tunable Kekulé reconstruction has been observed in all the studied areas of in total three different samples, including the sample in which we previously studied superconductivity¹³ (labeled sample C in this work). The large areas (that include more than twenty moiré sites) needed for unambiguously establishing IKS-order using the FT analysis outlined in Fig. 4 were studied in sample A and discussed in the main text. The presence of inter-valley coherence is also confirmed in the sample with a larger heterostrain (sample B).

Heterostrain extraction: The presence of heterostrain deforms the moiré lattice from an ideal equilateral triangular lattice. By experimentally measuring the two moiré lattice vectors g_1 and g_2 , we can extract the magnitude and direction of the heterostrain that best matches the observed moiré lattice geometry⁹ (see also SM section 3 for details of strain modeling). The magnitude of the heterostrain is uniquely determined from the moiré lattice constants l_1 , l_2 and l_3 labeled in Fig. 1b—we obtain a magic angle of $1.60^{\circ} \pm 0.01^{\circ}$ and strain magnitude $|\epsilon| = (0.12 \pm 0.04)$ %. We note that twist angle and strain were extracted using large uniform areas (typically at least $30 \times 30 \text{ nm}^2$) containing tens of moiré sites. This minimizes any errors that could potentially arise from imperfections due to the piezo scanner tube (such as, for example, the piezo creep effect).

The extraction of the strain direction is additionally sensitive to the twist-angle direction (clockwise vs counter-clockwise), as well as which layer experiences compressive strain. In our experiment, we stacked twisted trilayer graphene such that the middle layer is rotated counter-clockwise with respect to the top and bottom layers. We then extract the direction of the moiré lattice vectors g_1 and g_2 by comparing to an armchair direction of graphene, or equivalently to the G_1 vector in the FT. This information lets us to conclude that the middle layer experiences compressive strain (corresponding to negative ϵ in our conventions). With these additional pieces of information, the strain magnitude $\epsilon = -(0.12 \pm 0.04)$ % strain angle $\varphi = (87 \pm 10)^{\circ}$ are extracted. Same method has been utilized to sample B and sample C. From sample B we got strain magnitude $\epsilon = -(0.28 \pm 0.04)$ % and strain angle $\varphi = (138 \pm 10)^{\circ}$. From sample C we got strain magnitude $\epsilon = -(0.11 \pm 0.04)$ % and strain angle $\varphi = (60 \pm 10)^{\circ}$.

Kekulé auto-correlation analysis: Variation of the Kekulé pattern on the neighboring AAA sites is quantified by calculating the correlation between two small images taken at two spatially different parts of the large dI/dV map. The correlation, which we define as an element-wise multiplication between two same-sized images, is normalized such that it gives 1 for two identical images and -1 for fully reversed image. A 2D auto-correlation map plots the correlation between a fixed window, centered at a particular AAA site, and a moving window that spans the whole dI/dV map. The size of the window we choose to calculate the auto-correlation map in Fig. 3h is 1.2 nm; the result is insensitive to the size of the window within 0.8 nm to 1.7 nm.

A Kekulé dI/dV auto-correlation map calculates the correlation in a FT-filtered dI/dV map

that only contains signals that are periodic with the Kekulé wavevector. FT filtering is performed by first identifying six peaks corresponding to Kekulé distortion ($|K_i| = \frac{4\pi}{3\sqrt{3}a_0}$) and six peaks for graphene reciprocal lattice vectors ($|G_i| = \frac{4\pi}{3a_0}$). Six round masks of radius $3.5 \mathrm{nm}^{-1}$ centered around Kekulé (graphene) FT peaks are used to separate the desired signal from the rest of the data. An FT-filtered dI/dV map is produced by performing an inverse FT on a masked FT image. We calculate auto-correlation on the FT-filtered Kekulé dI/dV maps and plot only those peaks that are at local maxima in the graphene dI/dV auto-correlation map to trace the evolution of auto-correlation only when the two windows are atomically aligned.

Extraction of IKS wavevector: Because the IKS ground state is constructed by hybridizing the Kand K' valleys with a momentum mismatch q_{IKS} , FT peaks appear at $\gamma - \gamma' - q_{IKS}$ or equivalently at $\kappa_{top} - \kappa'_{top} - q_{\text{Kekul\'e}}$, rather than $\kappa_{top} - \kappa'_{top}$ for uniform Kekul\'e distortion (see Fig. 4h). We extract the IKS wavevector $q_{\rm IKS}$ or equivalently $q_{\rm Kekul\acute{e}}$ by measuring how much the FT peaks are offset from $\kappa_{top} - \kappa'_{top}$. While in theory, the vector $\kappa_{top} - \kappa'_{top}$ can be easily deduced from graphene reciprocal lattice vector peaks in the FT, small uncertainty in piezo calibration and the effect of strain makes it hard to distinguish the central graphene reciprocal lattice vector peak among many satellite peaks with similar intensities. Although neighboring satellite peaks at G_i are separated by one moiré reciprocal lattice vector g, their high-order counterparts at NG_i are apart by Ng. If our choice of exact G_i is off by g, the exact $3G_i$ will be located 3g away from the current G_i (marked as the yellow circle in the Extended Data Fig. 6), which is unlikely considering that the prominent satellite peaks locate within $\pm 2g$ from the center of the cluster. Our choice of G_1 and G_2 in Fig. 4b,c is the only choice that yields high-order FT peaks at $mG_1 + nG_2$ (m, n are integers from -3 to +3); G_3 is automatically determined by $G_3 = G_2 - G_1$ because we only have two independent reciprocal lattice vectors. The plotted G_3 (black circle in Fig. 4d) is precisely on top of an FT peak, consistent with the fact that we do not observe other long-wavelength patterns in FT-filtered 'graphene' dI/dV maps. Once we determine which FT peak corresponds to the exact G_i , the naively expected Kekulé FT peak positions (which would occur for T-IVC order) are calculated as $K_1 = (G_1 + G_2)/3$, $K_2 = (G_2 + G_3)/3$, and $K_3 = (G_3 - G_1)/3$. Note that, any FT peak can be chosen to calculate $q_{\text{Kekulé}}$, defined as the momentum separation from the calculated K_i modulo a moiré reciprocal lattice vector g. Wavevectors are only defined modulo moiré reciprocal lattice vectors – which are precisely identified as the momentum distance between the satellite peaks observed in Fig. 4 and thus any choice of reference moiré peak will yield a physically equivalent result. A particular FT peak is chosen to calculate $q_{\rm Kekul\acute{e}}$, so that the norm of $q_{
m Kekul\acute{e}}$ does not exceed the norm of g and the gate dependence of $q_{
m Kekul\acute{e}}$ can be traced continuously. Also, three $q_{\text{Kekul\'e}}$ can be extracted separately from K_1 , K_2 , and K_3 , and all three values match within the experimental range of error.

Kekulé wavevector error comes from locating the exact center of the FT peak with a finite width, which has intrinsic uncertainties coming from the measurement resolution and error due to the broadening of the peaks due to structural inhomogeneity. By taking a much larger map in the same area ($150 \times 150 \text{ nm}^2$, not shown), we verified that FT peaks are not limited by the structural inhomogeneity and set by the measurement resolution. We estimate the error bars in Fig. 4i,l the error bars are set by the pixel size and given by given as $\sqrt{2} \times 0.09nm^{-1} = 0.12nm^{-1}$, where $0.09nm^{-1}$ is half of the pixel size in Fig. 4b-g.

Inter-valley coherence in MATTG and other graphene-based systems:

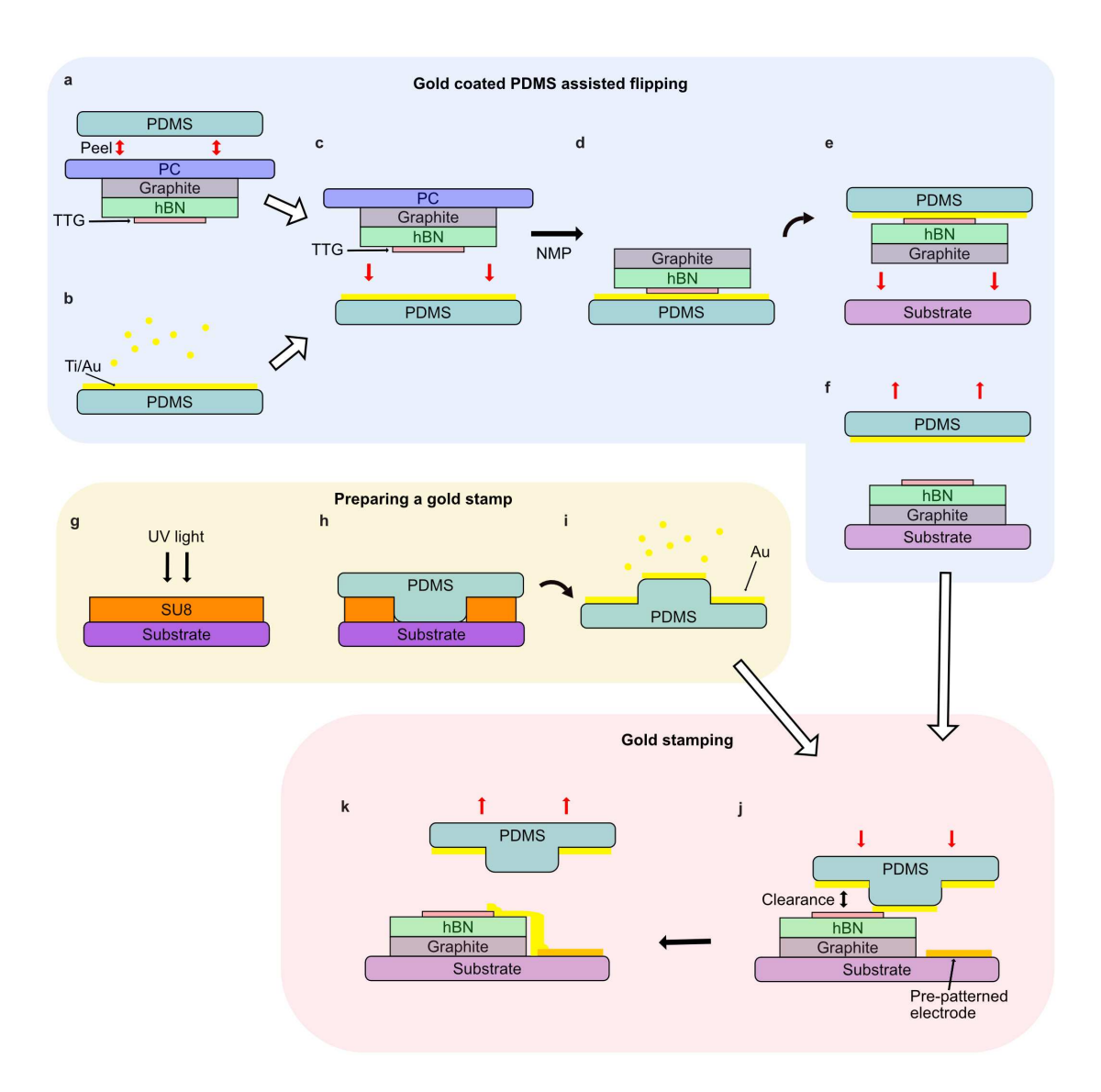
While many twisted graphene-based platforms have been proposed so far, the family of alternating-twist multilayers (including TBG and TTG) stand out due to their common set of symmetries and similar experimental phenomenology. In this context, the observation of the IVC order in MATTG can be understood to originate from the flat band sector of the TBG-like bands

(see SI for further details). We note, however, that due to the smaller moiré unit cell, the effect of strain and correlations in the two systems slightly differ, and consequently, the direct comparison of Kekulé reconstruction details and its doping dependence here and in Ref. have not be straightforward. In a more general context of moiré structures, apart from MATBG, the structure of the flat bands in other moiré systems can be very different, and as such, it is an interesting open question for future investigations if the IVC order is established in those systems as well. Finally, we note that recently IVC is also reported in monolayer graphene placed in high magnetic fields. While at first glance, the phenomenology, in general, is similar to the moiré systems as both platforms exhibit spontaneous breaking of valley-charge conservation due to strong electronic interactions, the monolayer graphene experiment is different in a number of fundamental ways. Perhaps the most important is that it takes place in the quantum Hall regime, where the non-interacting theory is described by Landau levels, and the time-reversal symmetry is broken.

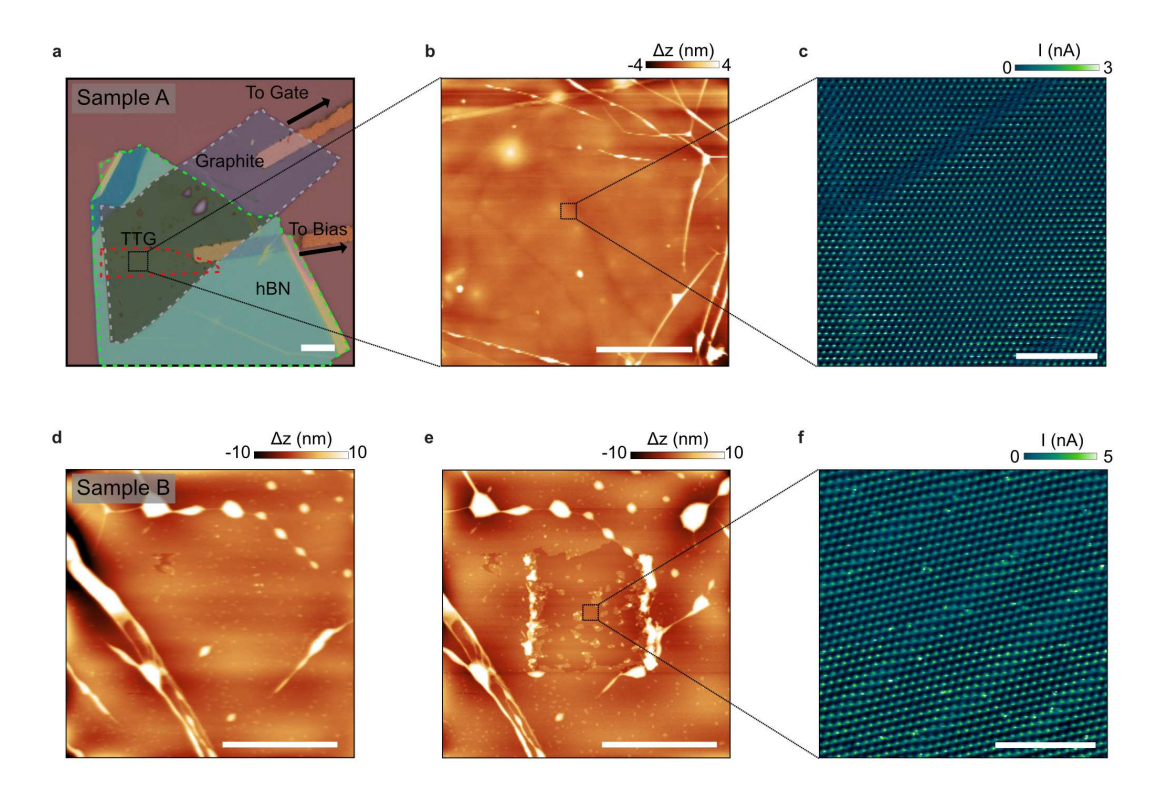
Acknowledgments: We thank Nick Bultinck, Sid Parameswaran, Abhay Pasupathy, Ashvin Vishwanath, Senthil Todadri, and Ali Yazdani for fruitful discussions. We are grateful in particular to Tomohiro Soejima and Mike Zaletel for pointing out subtleties regarding the extraction of q_{IKS} through Fourier analysis. Funding: This work has been primarily supported by National Science Foundation (grant no. DMR-2005129); Office of Naval Research (grant no. N142112635); and Army Research Office under Grant Award W911NF17-1-0323. S.N-P. acknowledges support from the Sloan Foundation. J.A. and S.N.-P. also acknowledge support of the Institute for Quantum Information and Matter, an NSF Physics Frontiers Center with support of the Gordon and Betty Moore Foundation through Grant GBMF1250; É. L.-H. and C.L. acknowledge support from the Gordon and Betty Moore Foundation's EPiQS Initiative, Grant GBMF8682 (at Caltech). C.L. acknowledges start-up funds from Florida State University and the National High Magnetic Field Laboratory. The National High Magnetic Field Laboratory is supported by the National Science Foundation through NSF/DMR-1644779 and the state of Florida. A.T. and J.A. are grateful for the support of the Walter Burke Institute for Theoretical Physics at Caltech. H.K. acknowledges support from the Kwanjeong fellowship. L.K. acknowledges support from an IQIM-AWS Quantum postdoctoral fellowship. Work at UCSB was supported by the U.S. Department of Energy (Award No. DE-SC0020305) and by the Gordon and Betty Moore Foundation under award GBMF9471. This work used facilities supported via the UC Santa Barbara NSF Quantum Foundry funded via the Q-AMASE-i program under award DMR-1906325.

Author Contribution: H.K. and Y.C. fabricated samples with the help of Y.Z., H.Z. and L.H., and performed STM measurements. H.K., Y.C., and S.N.-P. analyzed the data with the help of L.K. and E.B. E. L.-H., C.L. and A.T. provided the theoretical analysis supervised by J.A. S.N.-P. supervised the project. H.K., Y.C., E. L.-H., C.L., A.T., J.A., and S.N.-P. wrote the manuscript with input from other authors.

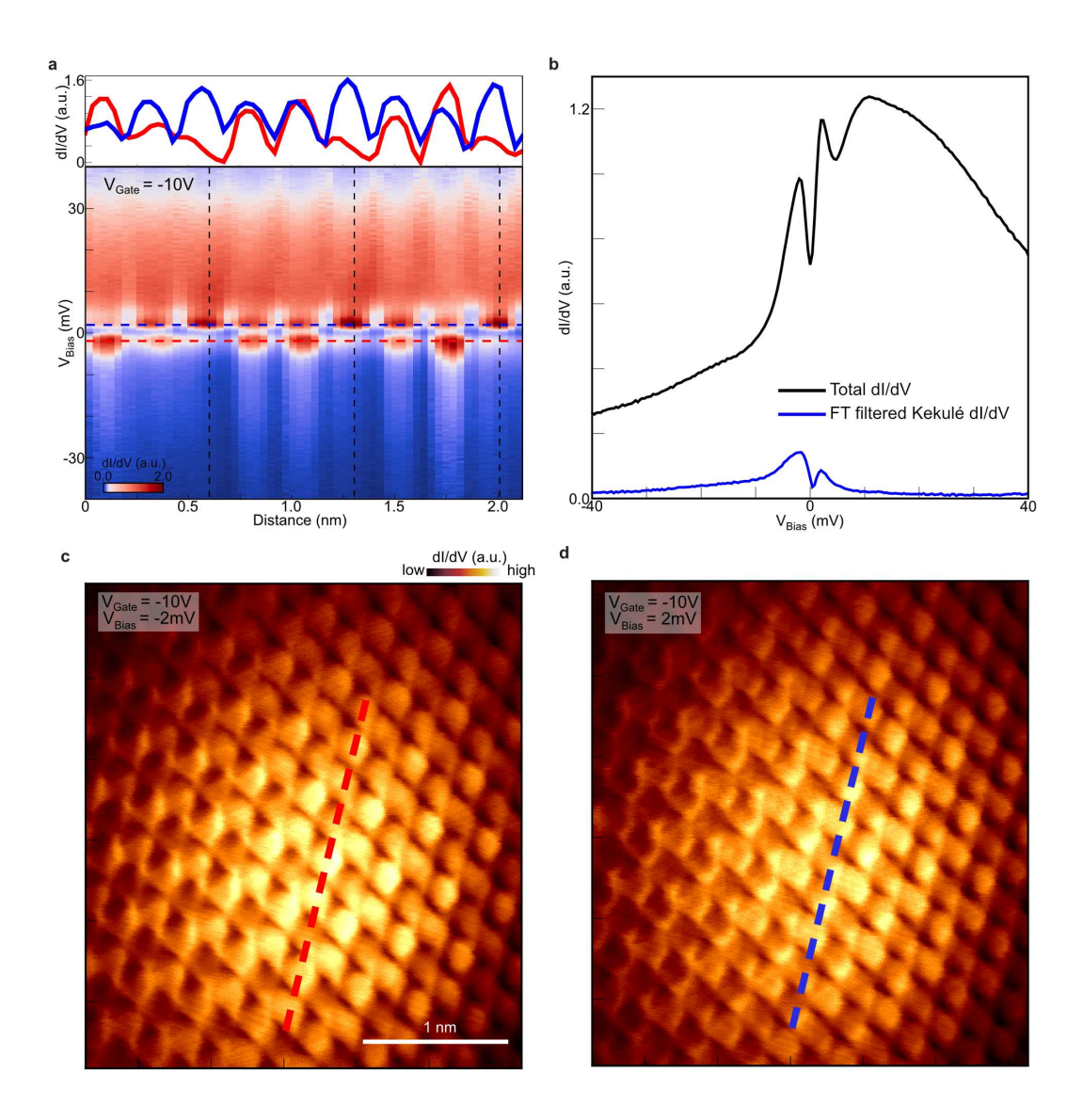
Data availability: The raw data shown in the main figures are available at Zenodo. Other data and code that support the findings of this study are available from the corresponding authors on reasonable request.



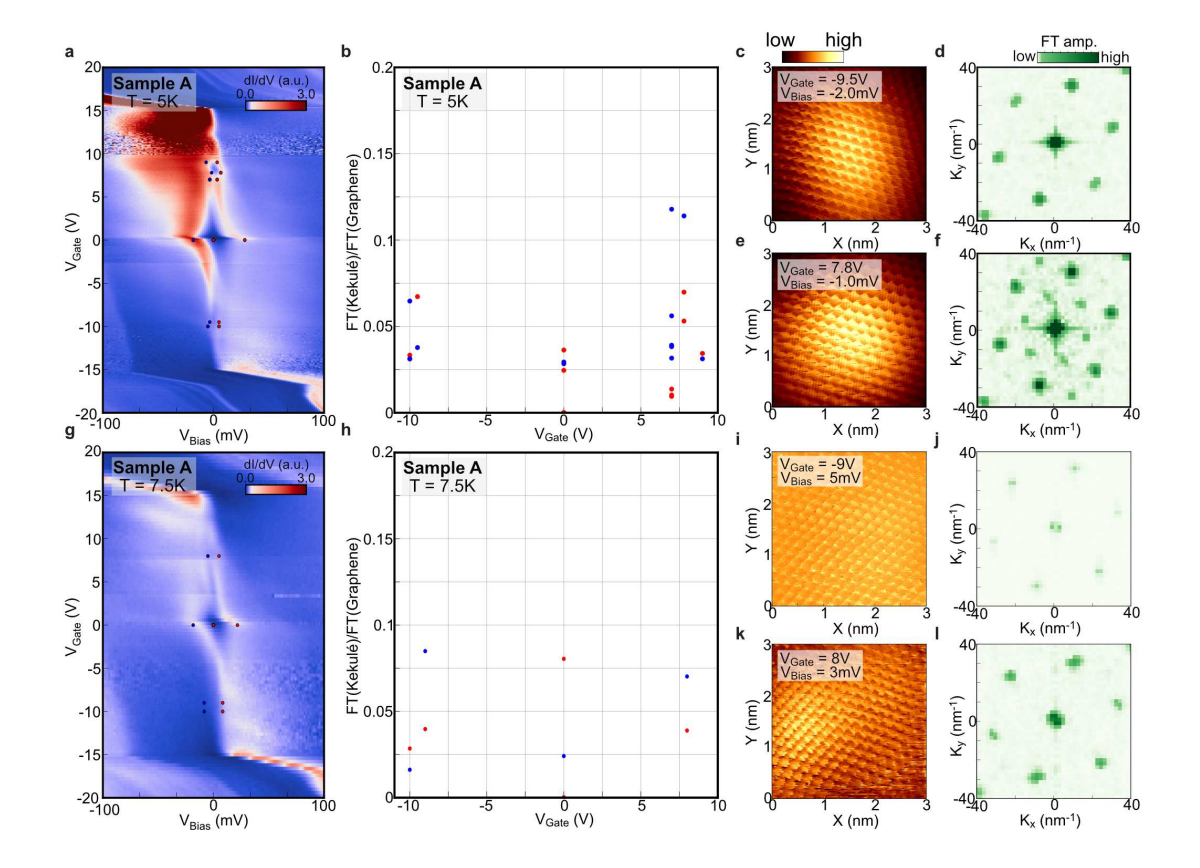
Extended Data Fig. 1. **Sample fabrication. a-f**, gold coated PDMS assisted flipping. A stack with PC film is peeled off from a PDMS block (**a**). A separate PDMS block is Ti/Au coated (**b**). Then the stack is put down to the gold coated PDMS (**c**). PC film is dissoved by NMP (**d**), before the stack is dropped down to a substrate (**e,f**). **g-i**, a gold stamp is prepared. A mold is defined by photolithography (**g**). PDMS is poured on the mold (**h**), and peeled off. Au is deposited on the stamp (**i**). **j,k**, the gold stamp is pressed down onto a desired area of the sample (**j**), leaving a gold strip that connects the sample and a pre-patterned electrode on the substrate (**k**).



Extended Data Fig. 2. AFM images of samples A and B. a, Optical microscope image of Sample A. b, AC tapping mode AFM image after the contact mode cleaning the $2 \times 2\mu m^2$ area around the center of the image. No sign of residue is found. c, cAFM image showing moiré pattern of MATTG. d,e, AC tapping mode AFM images of Sample B before (d) and after (e) cleaning. The residue boundaries after the cleaning indicate significant amount of residues on the surface. f, cAFM image. Scale bars: $10\mu m$ (a), $2\mu m$ (b,d,e), 100nm (c,f).

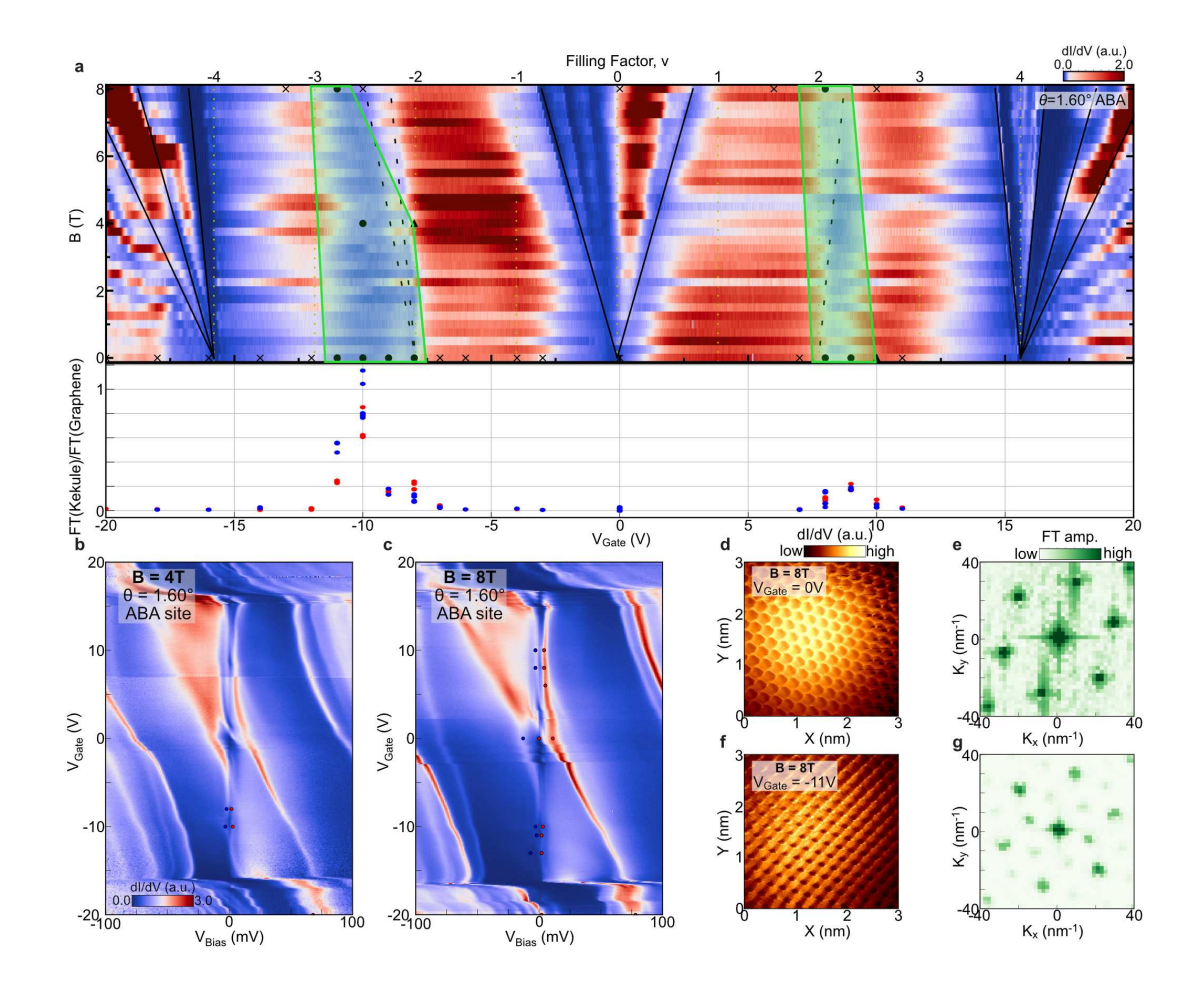


Extended Data Fig. 3. $V_{\rm Bias}$ dependent mapping of the lattice tripling order on MATTG. a, Conductance at $V_{\rm Gate} = -10 \rm V$ taken along spatial points and for range of $V_{\rm Bias}$. While at large positive $V_{\rm Bias}$, dI/dV shows periodic modulation that corresponds to graphene lattices, at low $V_{\rm Bias}$, additional periodic pattern that triples the graphene lattice periodicity is apparent. (black dashed lines) Upper inset shows two linecut taken at above ($V_{\rm Bias} = 2 \rm mV$) and below ($V_{\rm Bias} = -2 \rm mV$) E_F stressing lattice tripling. b, $V_{\rm Bias}$ spectroscopy extracted from Extended Data Fig. 3a that compares total dI/dV obtained by summing up along spatial coordinates and FT filtered Kekulé dI/dV which is a result of FT filtering on Extended Data Fig. 3a along spatial direction to extract Kekulé signal. ${\bf c,d}$, dI/dV map measured at fixed $V_{\rm Gate} = -10 \rm V$ at negative $V_{\rm Bias} = -2 \rm mV$ (${\bf c}$) and positive $V_{\rm Bias} = 2 \rm mV$ (${\bf d}$). Red and blue dashed line shows the spatial positions where Extended Data Fig. 3a is measured. Measurements are taken at $T = 400 \rm mK$.

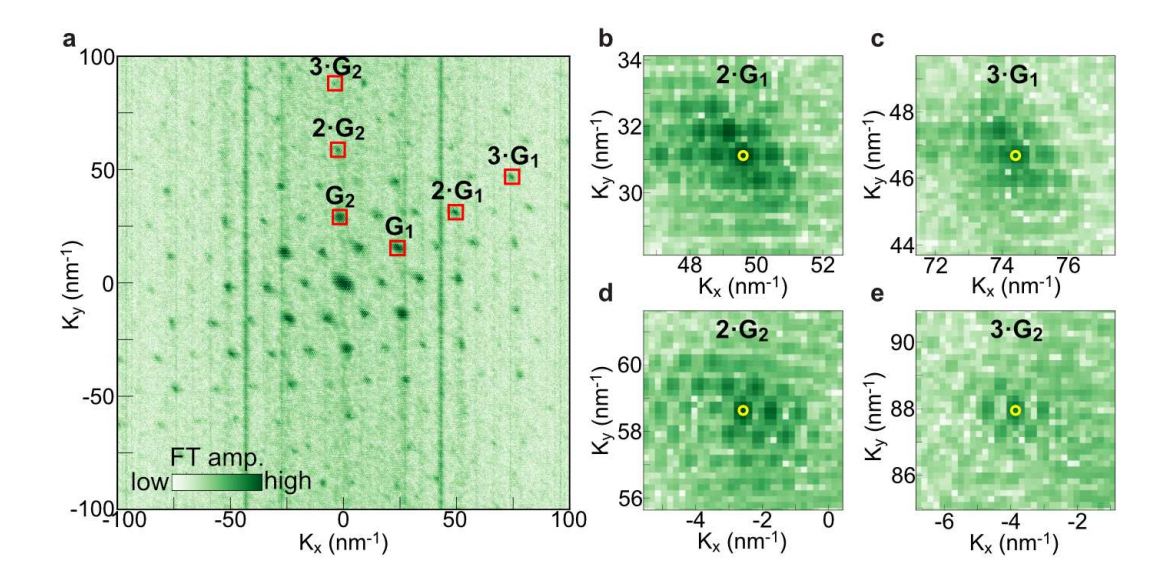


Extended Data Fig. 4. $V_{\rm Gate}$ dependent evolution of the lattice tripling order at higher temperatures.

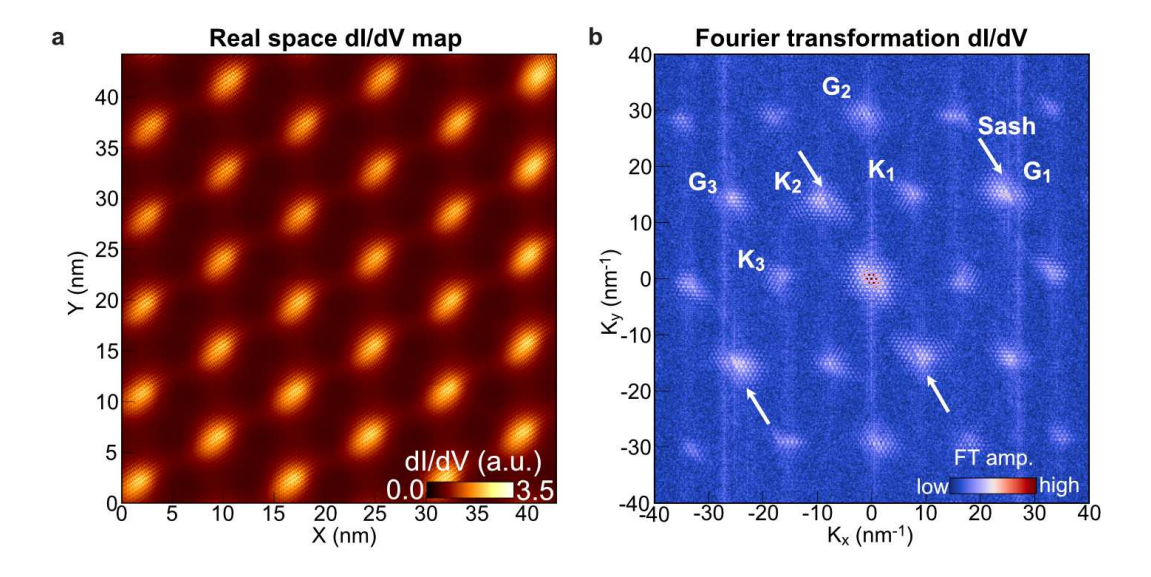
a, $V_{\rm Gate}$ dependent dI/dV spectroscopy measured at $T=5{\rm K}$ where $\nu=2$ correlated gap survives but gaps around $\nu=-2$ is greatly suppressed. Red (positive $V_{\rm Bias}$) and Blue (negative $V_{\rm Bias}$) dots marks the position where we measured 2D dI/dV maps. b, Intensity of the peak at Kekulé reciprocal lattice vector normalized by the intensity of the peak at graphene reciprocal lattice vector as a function of ${\bf V_{Gate}}$. c,e Real space dI/dV map at $V_{\rm Gate}=-9.5{\rm V}$ (c) and $V_{\rm Gate}=7.8{\rm V}$ (e). d,f Fourier transformation of Extended Data Fig. 4c,e. g, $V_{\rm Gate}$ dependent dI/dV spectroscopy measured at $T=7.5{\rm K}$ where $\nu=2$ correlated gap survives but gaps around $\nu=-2$ are greatly suppressed. Red (positive $V_{\rm Bias}$) and Blue (negative $V_{\rm Bias}$) dots mark the position where we measured 2D dI/dV maps. h, Intensity of the peak at Kekulé reciprocal lattice vector normalized by the intensity of the peak at graphene reciprocal lattice vector as a function of ${\bf V_{Gate}}$. i,j Real space dI/dV map at $V_{\rm Gate}=-9.5{\rm V}$ (i) and $V_{\rm Gate}=7.8{\rm V}$ (j). k,l Fourier transformation of Extended Data Fig. 4k,l.



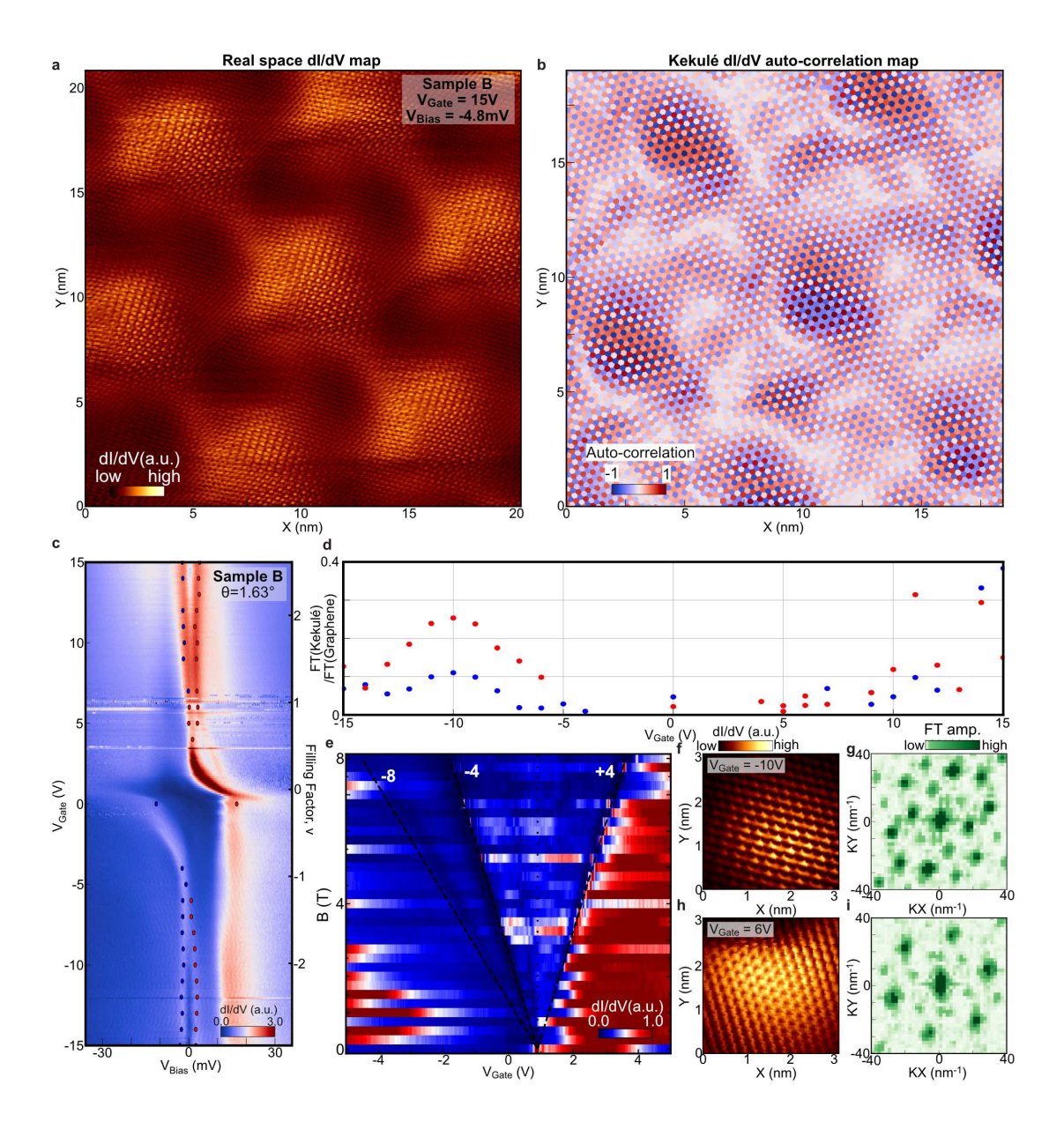
Extended Data Fig. 5. Out-of-plane magnetic field dependence of lattice tripling order. a, LDOS Landau fan diagram measured on an moiré ABA site. The lower panel shows intensity of the lattice tripling signal as in Fig. 2. Black circles marked on Landau fan indicate $V_{\rm Gate}$ and B, where we observe Kekulé peaks in FT. The black cross indicate values of $V_{\rm Gate}$ and B where we measured dI/dV map but could not observe Kekulé peaks in FT. The green polygon is an eye guide covering black circles and roughly denotes where we observed lattice tripling. b, c, $V_{\rm Gate}$ dependent dI/dV spectroscopy measured at B=4T (b) and B=8T (c). d, e, Real space dI/dV map (d) and corresponding Fourier transformation (e) showing the absence of Kekulé FT peaks around CNP at B=8T. f, g, Real space dI/dV map (f) and corresponding Fourier transformation (g) taken at B=8T that shows Kekulé order at $V_{\rm Gate}=-11V$.



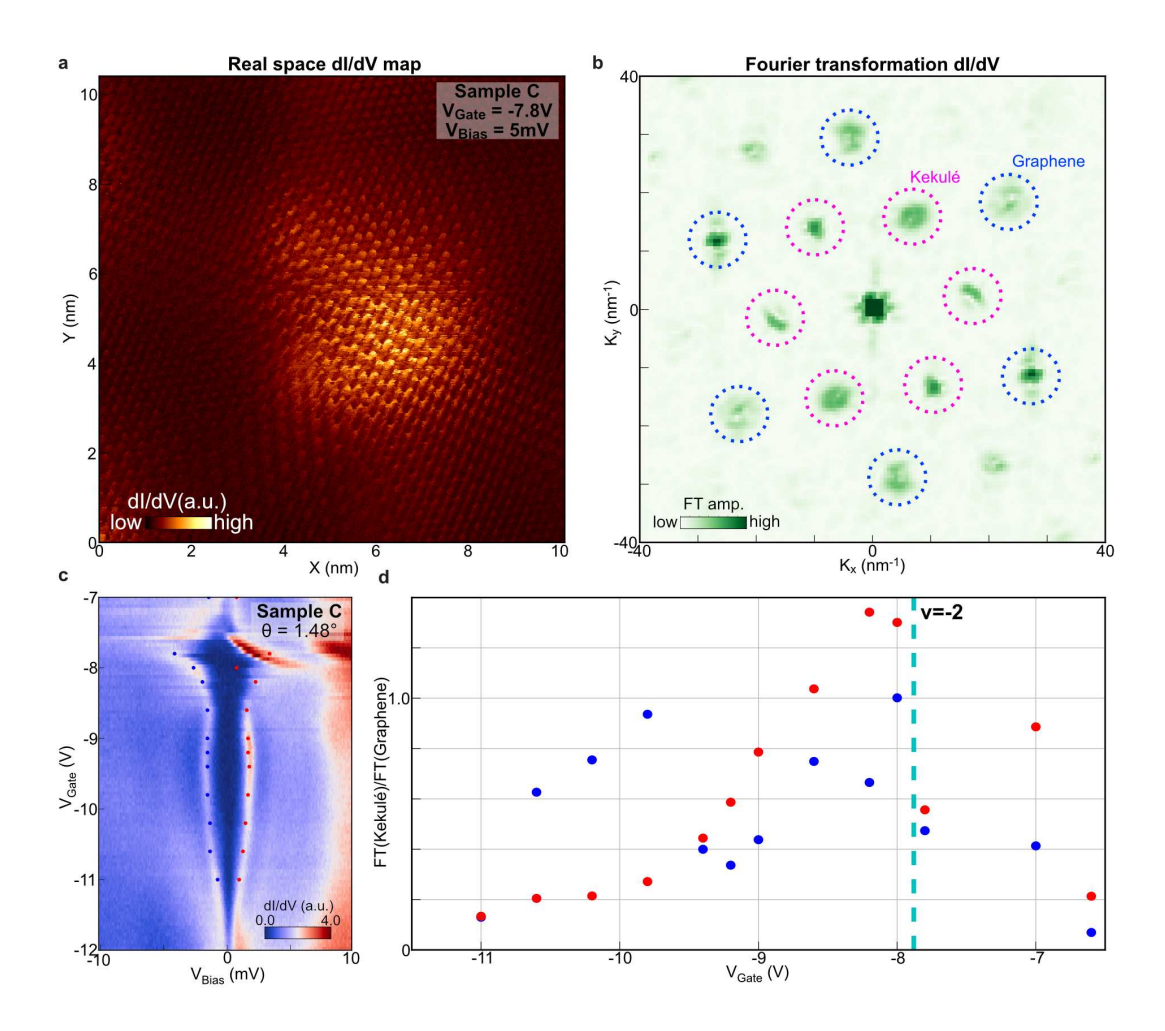
Extended Data Fig. 6. High-order graphene reciprocal lattice vector peaks from FT map at $\nu=-2.3$. a, Fourier transformation of the real space dI/dV map at $V_{\rm Gate}=-9{\rm V}$ and $V_{\rm Bias}=-2{\rm mV}$ showing larger momentum range compared to Fig. 4a. b-e, Zoom-in of the Extended Data Fig. 6a around $2G_1$ (b), $3G_1$ (c), $2G_2$ (d), $3G_2$ (e) that is marked as a red rectangle in Extended Data Fig. 6a. Position of NG_i that is determined from the positions of G_1 and G_2 from Fig. 4b,c is plotted as yellow circles which matches well with the FT peaks.



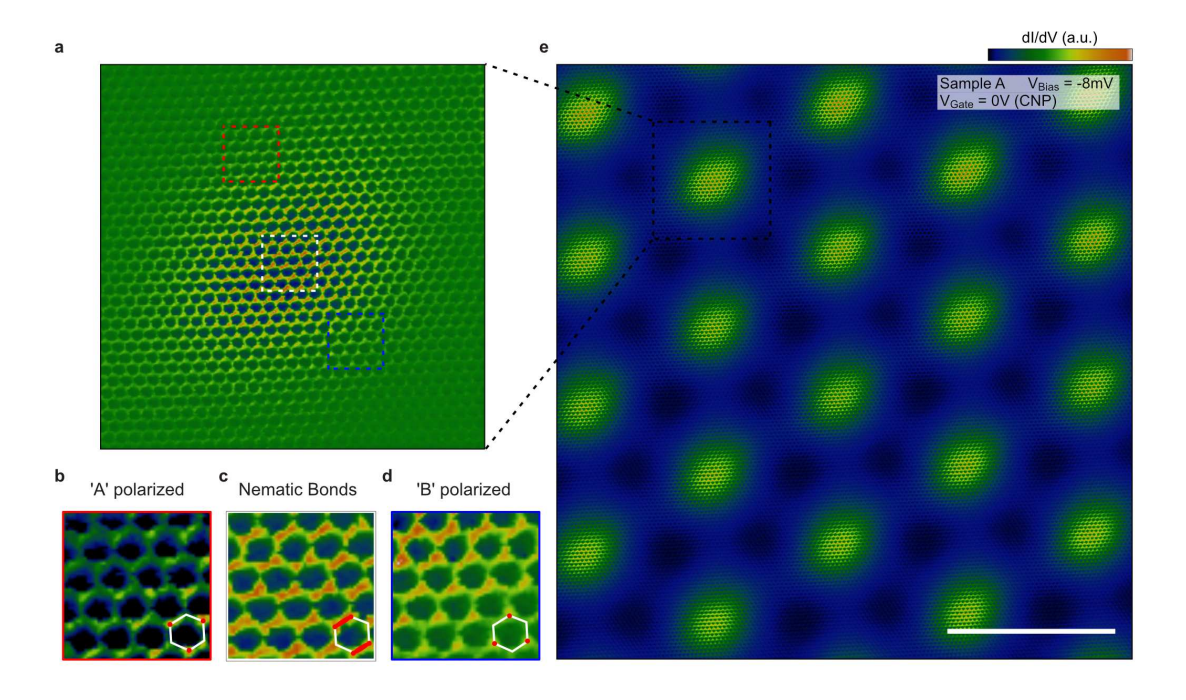
Extended Data Fig. 7. 42 nm by 42 nm size dI/dV map with Fourier transformation at $\nu=-2.3$ showing sash features. a,b, Real space dI/dV map (a) and corresponding Fourier transformation (b) taken at $V_{\rm Bias}=-2$ mV. White arrows point to the 'sash' features.



Extended Data Fig. 8. Lattice tripling order observed in sample B. a, Real space dI/dV map taken at $V_{\rm Gate}=15{\rm V}$ and $V_{\rm Bias}=-4.8{\rm mV}$ that includes seven moiré AAA sites. The area has twist angle of $\theta=1.59^{\circ}$ and heterostrain of $\epsilon=0.28\%$. b, Kekulé auto-correlation map created from real space dI/dV map in Extended Data Fig. 8a. Neighboring AAA sites are mapped with different colors, exhibiting the change in Kekulé patterns. c, $V_{\rm Gate}$ dependent dI/dV spectroscopy measured on sample B. d, $V_{\rm Gate}$ dependence of the Kekulé peak intensity in FT images normalized by the graphene lattice peak. Red (Blue) dot corresponds to positive (negative) $V_{\rm Bias}$, and is marked in Extended Data Fig. 8c. e, LDOS Landau fan diagram measured on sample B. Landau level degeneracies at each insulating dip is written in white numbers. f, g, Real space dI/dV map (f) and Fourier transformation (g) taken at $V_{\rm Gate}=-10{\rm V}$ showing lattice tripling. h, i, Real space dI/dV map (h) and Fourier transformation (i) taken at $V_{\rm Gate}=19{\rm V}$. Measurements are taken at $T=2{\rm K}$.



Extended Data Fig. 9. Lattice tripling order observed in sample C. a, Real space dI/dV map on one moiré AAA site measured at $V_{\rm Gate}=-7.8{\rm V}$ and $V_{\rm Bias}=5{\rm mV}$ which is at $\nu=-2$. The area has twist angle of $\theta=1.48^{\circ}$ and heterostrain of $\epsilon=0.08\%$. b, Fourier transformation of Extended Data Fig. 9a exhibiting prominent Kekulé FT peaks. c, $V_{\rm Gate}$ dependent dI/dV spectroscopy focusing on the correlated gaps at $\nu=-2\sim-3$. d, $V_{\rm Gate}$ dependence of the Kekulé peak intensity in FT images normalized by the graphene lattice peak. Measurements are taken at $T=400{\rm mK}$. In this sample, in the same area, we have previously established the presence of superconductivity 13 .



Extended Data Fig. 10. Nematic semimetal phase at charge neutrality. $\bf a$, atomic resolution dI/dV map (background filtered) at an AAA site. $\bf b$ - $\bf d$, signatures of nematic seminetallic (NSM) ground state. The intensity of one bond is stronger than the other two bonds near the center of the AAA site ($\bf c$). The pattern slowly evolves into 'A' sublattice polarized state around the red boxed region ($\bf b$), while 'B' sublattice polarized state is dominant around the blue boxed region ($\bf d$), which agrees the prediction in Ref. 25. $\bf e$, (unprocessed) dI/dV map at $V_{\rm Gate}=0V$ (CNP) on the hole side ($V_{\rm Bias}=-8mV$) where ($\bf a$ - $\bf d$) are taken. Other AAA sites in this map also show similar behavior as ($\bf a$ - $\bf d$). This map and the map in Fig. 3 are taken at the same area, only having different gate and bias voltages. Scale bar: 10 nm.

Figure number	$V_{\mathrm{Gate}}\left(\mathbf{V}\right)$	$V_{ m Bias} ({ m mV})$
Fig. 2a	-20V	63mV
Fig. 2b	-10 V	-3mV
Fig. 2a	0 V	-13mV
Fig. 2b	9 V	3mV
Fig. 3a	-9 V	2mV
Fig. 4a	-9 V	-2mV
Fig. 4i	-7.75V	-2mV
Fig. 4i	-8.3V	-2mV
Fig. 4i	-8.6V	-2mV
Fig. 4i	-9 V	-2mV
Fig. 4i	-9 V	2mV
Fig. 4i	-9.35V	-2mV
Fig. 4i	-9.7V	-2mV
Extended Data Fig. 5d	0 V	11mV
Extended Data Fig. 5d	-11 V	-2mV
Extended Data Fig. 6a-e	-9 V	−2mV
Extended Data Fig. 7a-b	-9 V	−3mV
Extended Data Fig. 8f	-10 V	4mV
Extended Data Fig. 8f	6 V	0mV

TABLE I. Summary of V_{Bias} values used for the dI/dV maps in the main figures.